Supplementary material

Absolute proliferation and death rates in tissues revealed by single-cell transcriptomics

Jakob Rosenbauer[1,2], Sofie Blahova[1,2], Michael Hegemann-Jensen[1], Alper Eroglu[1,2], Rickard Sandberg[1], Antony Cougnoux[1,2], Jean Hausser[1,2,*]
[1]Department of Cell and Molecular Biology, Karolinska Institute, [2]SciLifeLab
*correspondence to jean.hausser@scilifelab.se

Materials and Methods

Reagents

The source and reference of all the reagents used are listed in Table S2-S4.

Cell culture

All the cells used were tested for mycoplasma contamination at their arrival and both the passage before cryostorage or defrost were in media containing 2% MycoXpert to prevent any contamination. All the cell lines were adapted to grow in DMEM containing 10% FBS and 100U/mL penicillin streptomycin antibiotic at 37 degrees C 5% CO2. The human cell lines maintained were A549 (non small cell lung cancer; gift from Pr Frisen laboratory, CMB, Karolinska Institutet, Sweden), MDA-MB-231 clone A, L and S (Triple negative breast cancer; each clone is extensively described in Mahmoud et al.[1]). The mouse cell line was 4T1.

Longitudinal microscopy

Cell suspension at 10^6 cells/mL with viability above 90% based on trypan blue staining were incubated with 1uL of CFSE for 15 minutes at 37 degrees C in the dark in 1mL of PBS. The cells were then washed once with 10 volumes of PBS and resuspended in culture medium at $5x10^4$ cells/mL. Two milliliters of this suspension was added in each well of a 6 well plate and incubated at 37 degrees C, 5% CO2. 60 images per well were acquired automatically at 24h, 32h, 48h, 56h and 72h using AxioObserver.Z1 (Zeiss) equipped with Colibri7 (Zeiss), 10X objective with 0.3 numerical aperture and a Hamamatsu C11440 camera (Hamamatsu) using Zen 3.8. The images (size = $1.3x1.3mm^2$) were exported as 16bits tiff at a resolution of 2048 x 2048 pixels and a scaling of 0.65um/pixel. CFSE fluorescence was excited with a 475nm LED module at 25% for 100ms. Bright Field was acquired using the light source at 3V for 30ms. For each cell line CellPose 2.0[2] was trained to segment the different cells based on bright field imaging from approximately 30 images. The masks were then applied to measure the CFSE fluorescence intensity per cell over time. For each image the cell count was recorded to estimate cell growth over time.

Microscopy image analysis

Dirty regions imaging ROIs in which the autofocus did not work or air bubbles were visible were excluded from the analysis. The selection of these regions was done manually.

Cell segmentation was performed using Cellpose. Three different classifiers (for MDA-MB-231, 4T1 and A549), were trained to detect the cell outlines from the brightfield images. Training was performed using the CellPose GUI and repeated until the automated segmentation could not be improved by manual segmentation (approximately 30 images per cell line).

Following this, the segmentation models were applied to all images. From segmented images, the number of cells as well as the integrated CFSE abundance per cell was quantified. The

integrated CFSE abundance for each cell was estimated as the sum of the CFSE intensity of all pixels segmented as that cell. CFSE per well was then defined as the median value of the integrated CFSE abundance per cell.

Accumulation of CFSE in the medium - resulting from cell lysis - was corrected by subtracting the local background of each cell. The local background was determined by averaging the CFSE intensities in a circle of 80 pixels around the cell center, excluding all pixels segmented as cells. This mean background CFSE concentration per pixel of the local background was then removed from the integrated intensity of the cell.

Estimating proliferation and death from longitudinal microscopy (cell counts and CFSE quantification)

Longitudinal microscopy produces two numbers: the number of cells $n(t)$ and the integrated CFSE signal $I(t)$. The number of cell n(t) can be written as

$$n(t) = x(t) + y(t) \qquad (1)$$

where $x(t)$ is the number of live cells and $y(t)$ is the number of dead cells per field of view at time t. We model the number of live cells as the result of division (rate β) and death (rate α):

$$x(t) = x_0 e^{(\beta-\alpha)t} \qquad (2)$$

Thus, from longitudinal data on the number of live cells x(t), we can estimate the growth rate b - a but not the proliferation and death rates. To remedy this, we model the integrated CFSE signal

$$I(t) = n(t)\, I_c(t) \qquad (3)$$

where $I_c(t)$ the average CFSE intensity per cell. To relate n(t) and I(t) to the proliferation and death rates, we model the (unobserved) number of dying cells y as increasing with the death rate α times the number of life cells x, and decreasing as dead cells lyse and are cleared at rate γ from the microscopy images:

$$y'(t) = \alpha x(t) - \gamma\, y(t) = \alpha\, x_0\, e^{(\beta-\alpha)t} - \gamma\, y(t) \qquad (4)$$

Solving this differential equation assuming no dead cells at seeding time $y(0) = y_0$ leads to

$$y(t) = \frac{\alpha x_0 e^{(\beta-\alpha)t}}{\beta-\alpha+\gamma} + \left(y_0 - \frac{\alpha x_0}{\beta-\alpha+\gamma}\right)e^{-\gamma t} \qquad (5)$$

From this, we can write $n(t)$ as:

$$n(t) = \frac{x_0}{\beta-\alpha+\gamma}\left((\beta + \gamma)e^{(\beta-\alpha)t} - \alpha\, e^{-\gamma t}\right) \qquad (6)$$

Next we model the average CFSE intensity per cell, which decays with each division, therefore

$$I_c(t) = I_0 e^{-\beta t} \qquad (7)$$

Thus $I(t)$ can be written as

$$I(t) = n(t)\, I_0 e^{-\beta t} \qquad (8)$$

Plugging in the solution for $n(t)$ yields

$$I(t) = I_0 \frac{x_0}{\beta-\alpha+\gamma}\left((\beta + \gamma)\, e^{-\alpha t} - \alpha e^{-(\beta+\gamma)t}\right) \qquad (9)$$

Thus, the integrated CFSE signal decays exponentially at a rate set by cell death (rate α), with a delay set by the proliferation β and the clearance γ rates: the slower growth and clearance, the longer the delay in decreasing CFSE.

Inference of the five parameters x_0, β, α, γ and I_0 from the time course data:

Parameters were optimized in log-space to ensure positivity. The log-likelihood function combined a Gaussian error model for both cell counts and intensities, scaled by the expected measurement error, and included a soft prior on γ - dead cells persist in the tissue for 10 hours before lysis +/- 5 hours - to regularize the fit:

$$L = -\frac{1}{2}\sum_t \frac{[n_t - n_t^{meas}]^2}{n_t+1} - \frac{1}{2}\sum_t \frac{[I_t - I_t^{meas}]^2}{(0.015 I_t)^2} - \frac{1}{2}\left(\frac{1/\gamma - 10}{5}\right)^2 \qquad (10)$$

where n_t^{meas} and I_t^{meas} are measured cell counts and intensities, respectively.

For each well, we performed 200 independent optimizations starting from initial guesses based on biologically plausible values ($I_0 = 3x10^6$, $x_0 = 80$, $\beta = \frac{1}{24}\, h^{-1}$, $\alpha = \frac{1}{30} h^{-1}$, $\gamma = \frac{1}{10} h^{-1}$) with Gaussian perturbations (σ=0.25 in log-space). The optimization was performed using `scipy.optimize.minimize` with the default method (quasi-Newton), up to 400,000 iterations.

The solution yielding the highest log-likelihood across all runs was selected as the best fit for that well. Parameter uncertainties were estimated from the square roots of the diagonal elements of the inverse Hessian matrix of the log-likelihood function, computed via `autograd.hessian`.

All computations were performed in Python using the Autograd library for automatic differentiation and NumPy for numerical operations.

10x Genomics-based single-cell RNA sequencing experiment of 6 cell cultures

The cell lines once in suspension were washed with PBS and pelleted by 5 minutes of centrifugation at 400g. The individual suspensions were filtered through a 35um mesh and their densities were adjusted to 10^6 cells/mL in PBS on ice. An equal volume of each suspension was pooled before being processed at the National Genomics Infrastructure (NGI, Scilifelab, Solna, Sweden). The cell processing consisted of proceeding with 10X Genomics V3.1 3' dual index protocol according to manufacturer instruction (10X Genomics) and the libraries produced were sequenced on a NovaSeq XPlus (Illumina). The Fastq files were analyzed using zUMIs using a combined mouse and human genome which was built with STAR and consisted of the genomes GRCh38 and GRCm38 (mm10), with additional barcode capture (see yaml files in Code repository).

The hashing barcodes were extracted using the tool UMIcountR29 and assigned to each cell. Based on the hashing barcodes and human and mouse gene usage per cell, cells were classified into the six conditions sequenced.

Smart-seq3xpress-based single-cell RNA sequencing of live, apoptotic and dead cells

To establish robust transcriptional signatures of dying cells, we performed single-well cell sorting followed by Smart-seq3xpress. 4T1, A549, MDA-MB-231 clone A, L and S were grown in cell culture medium. Adherent MDA-MB-231 clone L were grown with 1uM of Paclitaxel, a concentration we have previously shown to slow proliferation while retaining a viability compatible with the experiment[1]. The cells in culture were detached with Trypsin treatment for 3-5 minutes at 37 degrees C and the reaction was quenched by adding back the cells supernatant to conserve dead cells. The suspension was washed twice in PBS, 4 minutes at 400g. The cells were then labelled using the live/dead stain BOBO3 and apoptosis marker AnnexinV-APC following manufacturer's instruction. We isolated 3 cell populations on the basis of the BOBO3 and Annexin-V flow cytometry markers using an Aria3 flow cytometry with a 100um nozzle and low pressure settings. Live cells were gated as BOBO3- AnnexinV-, dying (early apoptotic) cells as BOBO3- AnexinV+ and dead cells (necrosis or late apoptosis) as BOBO3+ AnexinV+ (Fig. S2a-b). Individual cells were isolated in 384 well pcr-plates. After 10s centrifugation at 1000g the plates were sealed and stored at -80*C until processed using Smart-seq3xpress protocol[3]. All the reagents and bioinformatic pipeline related to Smart-seq3xpress are available online[4].

Defining robust transcriptional signatures of cell death

Dying cells were defined based on positivity for either BOBO-3 or Annexin IV, as well as those positive for both markers. Gene expression data from Smart-seq3 was normalized to 10,000 reads per cell - a figure often found in scRNAseq experiments - and subsequently log-transformed using the natural logarithm of (1 + x).

To identify genes differentially expressed between live and dying cells, we used the scanpy.tl.rank_genes_groups function using the 't-test' method for statistical testing. Following this, cells were randomly split into training and test sets, with 75% of cells allocated to the training set.

A logistic regression classifier (sklearn.linear_model.LogisticRegression) was trained on the normalized expression data, restricted to the top N differentially expressed genes between live and dying cells. Classifier performance was evaluated using sklearn.metrics.accuracy_score on both the training and test datasets. This procedure was repeated across a range of gene set sizes, varying N from 2 to 200 in steps of 15. Training accuracy increased with the number of genes N, as expected: more genes provide more features to the classifier (Fig. S3e). Test set accuracy initially increased for the same reason, before peaking and decreasing due to overfitting. We used N=122 as this value yielded highest accuracy on the test set, thus balancing accuracy and generalizability (Fig. S3e).

As datasets may differ in the number and identity of detected genes — due to differences in transcriptomic technologies, cell / tissue type, reference genome — the set of 122 genes may not suit all datasets. For example, death genes #31 and #73 could be missing from a new dataset to be analyzed, but this dataset features 30 other death-associated genes which were not selected among the top 122 genes above because including them leads to over-fitting. Can we use some of these 30 genes to compensate for missing genes #31 and #73 in the new dataset?
To address this, TIDYI performs the above-described gene selection and classifier training for each dataset. We first determine the set of genes common to the new dataset to be analyzed and to the Smart-seq3 scRNAseq data of sorted live vs dying/dead cells collected in the present study (Fig. S2). Among this set of common genes, the gene selection procedure of the previous paragraph is performed, optimizing test-set classification accuracy of life vs dying/dead cells in the Smart-seq3 scRNAseq data of Fig. S2. This ensures optimal selection of death genes for the new dataset.
Importantly for the applicability of TIDYI, no new tissue-specific sequencing of sorted live vs dying/dead cells is necessary for this procedure under the reasonable hypothesis that dying cells express similar genes across tissue types.

Calibrating a minimal mathematical model connecting cell dynamics and gene expression

To transform the fraction of proliferating and dying cells (unit: fraction, from scRNAseq) into rates of proliferation and death (unit: 1/time), we introduce a simple mathematical model that predicts the fraction of proliferating cells ρ_p and dying cells ρ_d among a group of cells in a scRNAseq sample, and from there, estimates the proliferation rate $\beta = \beta_0 \rho_p$, death rate $\alpha = \alpha_0 \rho_d$ and growth rate $\partial \ln(n)/\partial t = \beta - \alpha$ of this group of cells. The group of cells can be for example cells of a given type (CD8 T cells, macrophages, etc.), or cells belonging to a specific phenotypic cluster, or any meaningful set of cells defined by the analyst. The input groups of cells need to

be sufficiently large (100+ cells in our simulations) to estimate the fraction of proliferating and dying cells.

Our mathematical model hypotheses that the population-level proliferation rate β can be written as the fraction ρ_p of cells that express proliferation genes times the inverse time needed for a proliferating cell to divide β_0, $\beta = \beta_0 \rho_p$ (Fig. 1e). We hypothesized that a similar relationship – $\alpha=\alpha_0\rho_d$ – holds for the death rate. From the death rate, the half-life can be computed as $\log(2)/\alpha$.

To test both hypotheses and calibrate this model, both the proliferation rate β and the death rate α were measured in 6 conditions by longitudinal microscopy (Fig. 1d). To do so, the growth rate of the cell population was quantified from longitudinal measurements of cellular density. Death rates were estimated by initially labelling cells with CFSE (Thermo Fisher), a fluorescent dye that cannot be produced by cells and is lost by dilution in the medium when cells die[5]. Quantifying loss of CFSE over time revealed death rates. The difference between growth and death estimated proliferation.

The fraction of proliferating cells ρ_p was determined by scRNAseq in the same conditions, by screening pathway databases for gene sets whose expression scales linearly with the proliferation rates (Fig. 1f). Specifically, cell cycle-associated gene sets from the g:Profiler datasets CORUM, GO:BP, GO:MF, WP and REAC were scored as the sum of member genes log TPMs. This quantified the expression of each gene set in each cell of our dataset.
We selected the gene set that best predicted proliferation by training a two-parameter (bias, scaling) logistic regression classifier of proliferation which outputs the probability that a given cell is proliferating. Averaging these probabilities over all cells yields the proportion of proliferating cells ρ_p. Thus, we trained the two-parameter logistic regression model to optimize the correlation between ρ_p and proliferation rates measured by longitudinal microscopy.
Among all the gene sets we tested, genes related to the mitotic spindle assembly produced ρ_p that best correlated with longitudinal microscopy proliferation rates.

From these estimates of the proportion of proliferating and dying cells, the time to division β_0^{-1} (and time to death α_0^{-1}) were estimated by regressing β (α) on ρ_p (on ρ_d) across cell cultures.

As a control, since genes related to the mitotic spindle assembly are expressed in G2, ρ_p should represent the proportion of cells in G2 and the scaling constant β_0 should represent the inverse duration of the G2 phase. Indeed, the fitted β_0^{-1} (3.4h) matched previous experimental measurements (3.4-4.0h)[10].

A potential caveat is that G2 genes may faithfully capture proliferation in healthy cells but cells arrested in a specific phase of the cell cycle may express the same genes without actually proliferating. To address this, our rate and scRNAseq measurements include conditions leading to cell cycle arrest (low-serum, paclitaxel), to guide transcriptional signatures specific to cycling, non-arrested cells. The existence of such signatures is supported by the observation that Ki67 abundance and CDK2 activity differ in cycling vs arrested cells[11].

ρ_d was computed using the dying cells classifier (Fig. S4f).

Adapting TIDYI for mouse scRNAseq data

To perform TIDYI on mouse data, we adapted the proliferation classifier, the death classifier, and the scaling constants connecting the proportion of proliferation and dying cells with the respective rates.

For the division classifier, the same gene set and scoring - sum of logTPM - was used as for the human data, using the mouse orthologous gene names.

For the classifier of dying cells, we first identified top differentially expressed genes on the human scRNAseq data of live and dying/dead cells as described above. But we found that the weights of these genes in the logistic classifier had to be re-fitted because their abundance varied across species. To do so, we used mouse scRNAseq data of live and dying/dead cells. Here, again we varied the number of genes used and chose the classifier with the highest test set prediction accuracy. The resulting classifier was used to calculate the proportion of dying cells in the sample.

Finally, the two classifiers were applied on the mouse 10x sample to estimate the proportionality constants between the fitted proportions of proliferating and dying cells and the respective rates measured by longitudinal microscopy.

Mouse tumor growth measurement and scRNAseq profiling

To validate that TIDYI predicts the growth rate of tumors *in vivo*, we used data from Gsell et al.[6]. Briefly, mouse tumors were induced using an immunocompetent allograft breast cancer model. Cancer cells were modified to express luciferase to allow non-invasive longitudinal measurements of tumor size by bioluminescence imaging (BLI). Longitudinal BLI measurements were then used to compute the tumor growth rate at the time of tumor collection.

Single-cell RNAseq was performed on the collected tumors (n=2 tumors x 4 time points). Single-cell RNAseq from single tumors were analyzed to identify cell types[6]. TIDYI was performed on each cell type separately. The difference between the absolute proliferation and death rates of cancer estimated by TIDYI was used as a predictor of the tumor growth rate.

To compare predicted growth rates to the typical time-to-volume growth path of this mouse tumor model, time-to-BLI measurements from 47 tumors were smoothed, assigning the sizes to time bins and calculating the mean and confidence interval for each bin (shaded area of Fig. 2a).

While the maximal photon flux post luciferase injection measured by BLI is an established proxy for tumor volume, photon fluxes are less interpretable than tumor volumes. We thus converted photon fluxes [photon per second] into volume units. To do so, we used the property that photon flux scales linearly with tumor volume as measured by a caliper (not shown). Using paired measurements of photon flux by BLI vs tumor volume by caliper, we estimated a scaling

constant — 6.62×10^{-8} mm^3 / (photon/sec) — relating photon flux to volume by regression. This constant was used to rescale all photon fluxes into tumor volumes.

TIDYI in squamous cell carcinoma vs site-matched normal skin

Single-cell RNA sequencing data from GSE144240 were downloaded from GEO. Cell type annotation was performed using SingleR with the *BlueprintEncode* reference. Consensus cluster annotation was applied and TIDYI was performed on keratinocytes.

Spatial localization of TIDYI proliferation and death signatures in the gut epithelium

Visium spatial transcriptomics data from GSE158328 were downloaded from GEO. Spots outside the tissue were excluded by segmenting the H&E staining, and the dataset was subset to spots inside the tissue. Gene set scores for TIDYI's proliferation and death signatures were computed on log-transformed RNA counts using scanpy.tl.score_genes and visualized spatially.

The gut villi are organized with stem cells at the bottom of the crypt, which divide and differentiate into progenitors and finally into fully differentiated epithelial cells. Those epithelial cells migrate towards the top of the villi and eventually die and are shed into the lumen of the gut. Depending on the cut angle across the duct this transition from high proliferation in the crypt to high death at the top of the villi can be seen by spatial transcriptomics (cf. Fig S4 g)

TIDYI in Crohn's disease

The human single cell data was downloaded from GEO GSE134809 and intestinal samples were imported into Scanpy for downstream analysis. Cell type annotation was performed using the SingleR package with the 'blueprint_encode' reference dataset. To correct for batch effects, Harmony integration was applied, followed by unsupervised clustering. Cluster cell types were annotated based on consensus cell type labels derived from SingleR predictions. TIDYI was performed on epithelial cells and the proliferation and death rates compared across samples.

TIDYI of progenitor keratinocytes dynamics in young and aged skin

Single-cell RNA sequencing data from all five samples of GSE130973 were downloaded and log-transformed. The dataset included 5 skin samples from a sun-protected area: two from young donors (age: 25, 27 years), three from aged donors (age: 53, 69 and 70 years).

Batch effects were corrected using Harmony. Cell types were annotated according to expression of canonical marker genes: *COL1A1*, *COL1A2* (fibroblasts), *KRT15* (progenitor keratinocytes), *KRT10* (differentiated keratinocytes), *PMEL* (melanocytes), *CD3D*, *CD4*, *CD8A* (T cells), and *VWF* (endothelial cells). Based on marker profiles, cells were classified into the following categories: keratinocytes (differentiated and stem), melanocytes, T cells, endothelial cells, and fibroblasts. Following this TIDYI was run on the annotated datasets.

From the literature, we can estimate a possible range on the rate of proliferation of keratinocyte progenitors. In normal skin, Halprin[7] estimated that 40-56 days separate cell birth from reaching the outermost epithelial layer. Thus, progenitors need to divide at least once every 56 days, and most likely more often as there are several cell layers to populate between the basal layer and the outermost epithelial layer. Gelfant[8] estimated that stem cells divide less than once per 200h (8.3 days). This puts the division time of keratinocyte progenitors between 8.3 and 56 days, or equivalently proliferation rate in the $5x10^{-4}$ - $3x10^{-3}$ per hour range.

This example illustrates that TIDYI can estimate rates that are much slower than the cell cycle time. This is because TIDYI rates are estimated from the proportion of cells undergoing cell division / death. Thus, the number of cells in the dataset sets a lower bound for the slowest rates that can be estimated: more cells allow estimating slower rates.

Performing TIDYI on human blood peripheral immune cells

Raw UMI counts and author cell type annotation of the human PBMCs scRNAseq experiment of Elz et al. were downloaded from GEO accession GSE295527.
The data consists of cells from two healthy donors, each split into two cell suspensions. Each suspension was sequenced both with the GEM-X (v4.0) and NextGEM (v3.1) protocols (10x Genomics).
Datasets from each protocol underwent quality control separately. In each dataset, cells with at least 100 UMIs and genes expressed in at least 3 cells were retained for further analysis. Of these, top and bottom 1% quantile of cells in terms of total UMI counts were filtered out.

Not all cells were annotated by the authors - presumably dying and dead cells were excluded from original cell annotation. Yet, these cells convey information about the death kinetics of blood immune cells. In order to type cells left unannotated by the authors, we performed PCA on log gene expression (log TPM normalization[9]), using a number of top PCs equal to 1/100th of the number of cells in the dataset. The k=30 nearest neighbors of each cell were determined and used to find cell clusters using the Leiden algorithm[10] (resolution: 0.1). Cells with no author-supplied annotation were assigned to the majority-voted cell type of their assigned cluster.

We performed TIDYI twice, once per dataset (that is once per protocol), on the raw UMI counts and genes found in that protocol, and stratified the proliferation and death estimations by cell type, technical replicate and donor. Only cell type, replicate and donor triplets with at least 50 cells were retained.

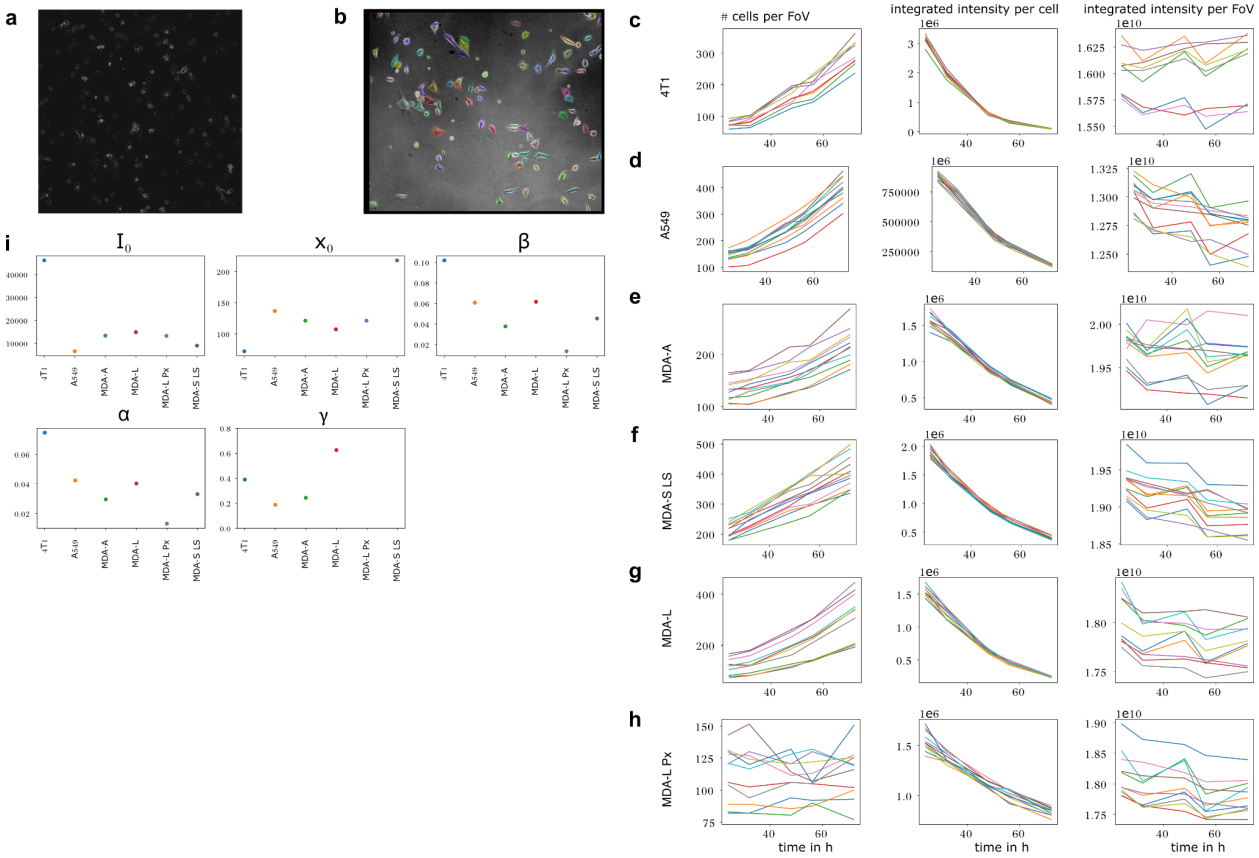

Figure S1 Proliferation and death rates in 6 cell cultures by longitudinal microscopy. **(a)** Representative brightfield image. **(b)** Example of segmentation of the brightfield image by CellPose. Each segmented cell appears in a different color. **(c-h)** Per well time dynamics of the number of cells per field of view (FoV), median CFSE intensity per segmented cell which are used as inputs of the model. The integrated image intensity per FoV stays roughly constant and is shown here as a validation of our model assumption that the total CFSE signal is conserved, except for signal loss through cell death.. These are used as an input to infer cell dynamics parameters - proliferation, death, and more (see panel i). **i.** Model parameters inferred from the longitudinal microscopy data of panels c-h. Parameters are defined in Equation 9 (Methods). I_0: median CFSE intensity per cell at time t=0h. x_0: number of cells per field of view at time t=0h. β: proliferation rate, unit: 1/h. α: death rate, unit: 1/h. γ: clearance rate of dead cells, unit: 1/h.

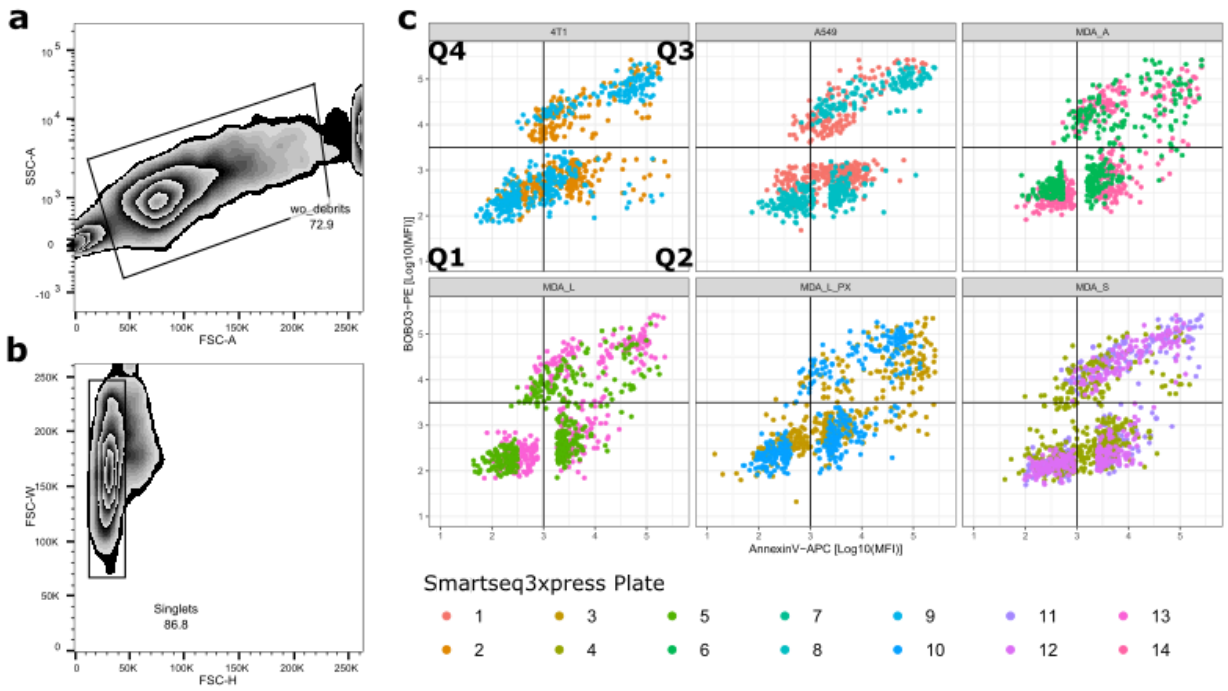

Figure S2 To define a transcriptional signature of cell death independently of the death pathway, we performed scRNAseq on sorted populations of live vs dying/dead cells. (a) Cells were gated to remove small size debris and clumped cells. **(b)** Following that, cells were gated to remove doublets. **(c)** Subsequent gating defined define live (Q1, AnnexinV_APC- BOBO3-), early apoptotic (Q2, AnnexinV_APC+ BOBO3-), late apoptotic (Q3, AnnexinV_APC+ BOBO3+) and necrotic (Q4, AnnexinV_APC- BOBO3+) cells for each cell line. Different plates contributed to all live-dead states. The high prevalence of dead/dying cells originates is due to us intentionally enriching them by FACS, not to low viability in the cell cultures. Panel: cell culture. Colors: 384-well Smartseq3xpress plate. PX = 1μM paclitaxel.

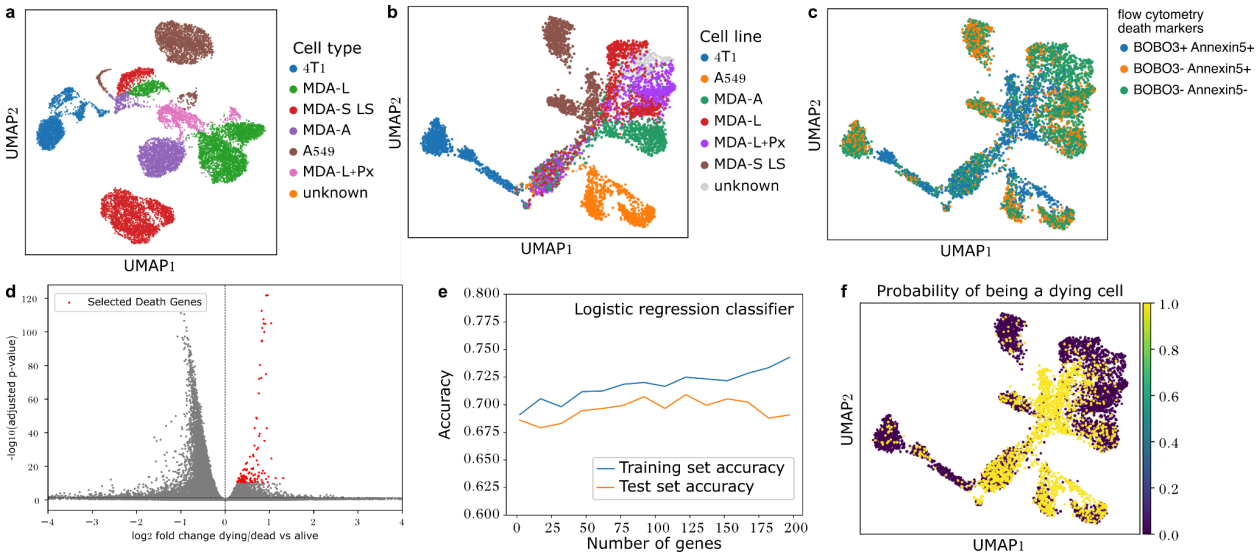

Figure S3 Expression of 122 genes discriminated and optimally classified live vs dead and dying cells across the 6 cell cultures. (a) UMAP projection of single-cell transcriptomes from 3' end gene expression profile (10x Genomics) used to associate transcriptomes to proliferation and death rates. Single-cells cluster by cell lines and growth condition, as expected from a successful scRNAseq experiment. Unknown cell type: for a small fraction of cells, the multiplexing barcode could not be sequenced. These cells could thus not be assigned to their condition and were discarded. **(b)** To identify generic transcriptional signatures of dying and dead cells, live and dying/dead cells were isolated by FACS (Fig. S2c) and their transcriptomes profiled by SmartSeq3xpress profiling. Unknown cell type: for a small fraction of cells, the well barcode could not be sequenced. These cells could thus not be assigned to their condition and were discarded. Axes: UMAP projection. Color: cell culture. **(c)** Same as b., but colored by markers of apoptosis (Annexin5) and necrosis (BOBO3). **(d)** Comparing expression in dying/dead cells vs live cells identified genes consistently up-regulated in dying/dead cells across cell cultures. P-value from t-test. **(e)** From co-profiling of cell death markers and single-transcriptomes, a logistic regression model was trained to classify live vs dying/dead cells based on gene sets of increasing size. A set of 122 genes achieved highest accuracy on the test set. **(f)** The probability of being a dead cell estimated by the logistic regression model overlaps with flow cytometry markers of dying dead cells (panel c).

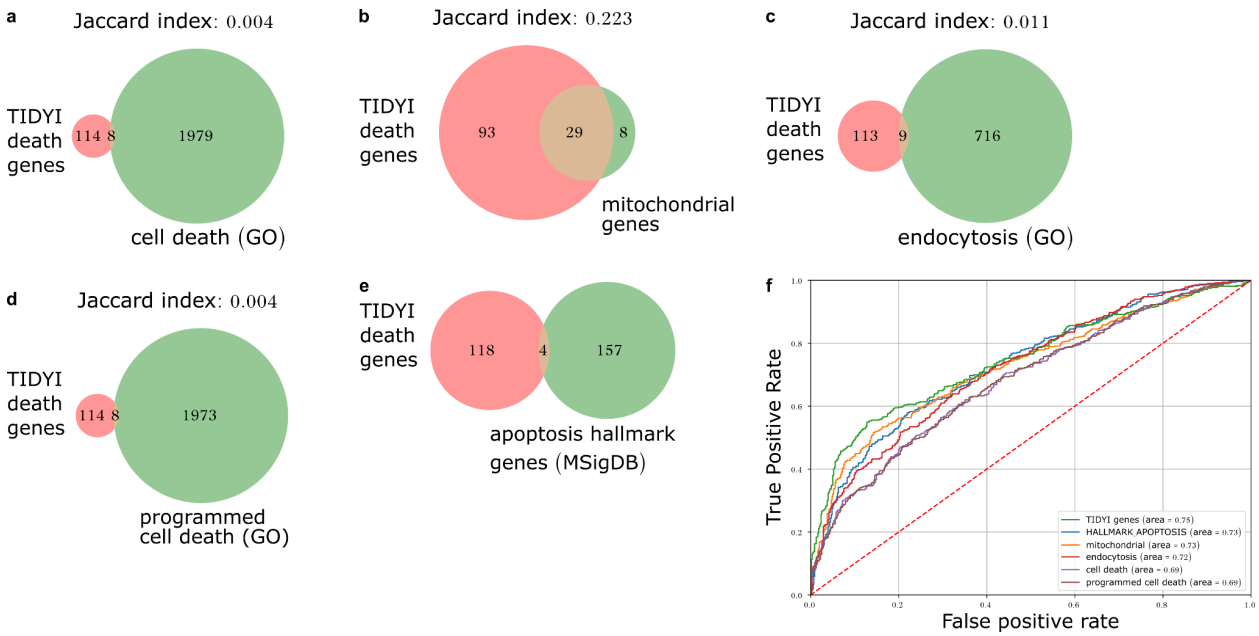

Figure S4 (a-e) The 122 genes that discriminate and optimally classify live vs dead/dying cells across the 6 cell cultures (Fig S3) show low overlap with cell death genes, and overlap with previously identified markers of low-quality cells (mitochondrial genes). **(f)** The 122 gene signature best classifies dead/dying cells vs live cells out of other established gene signatures.

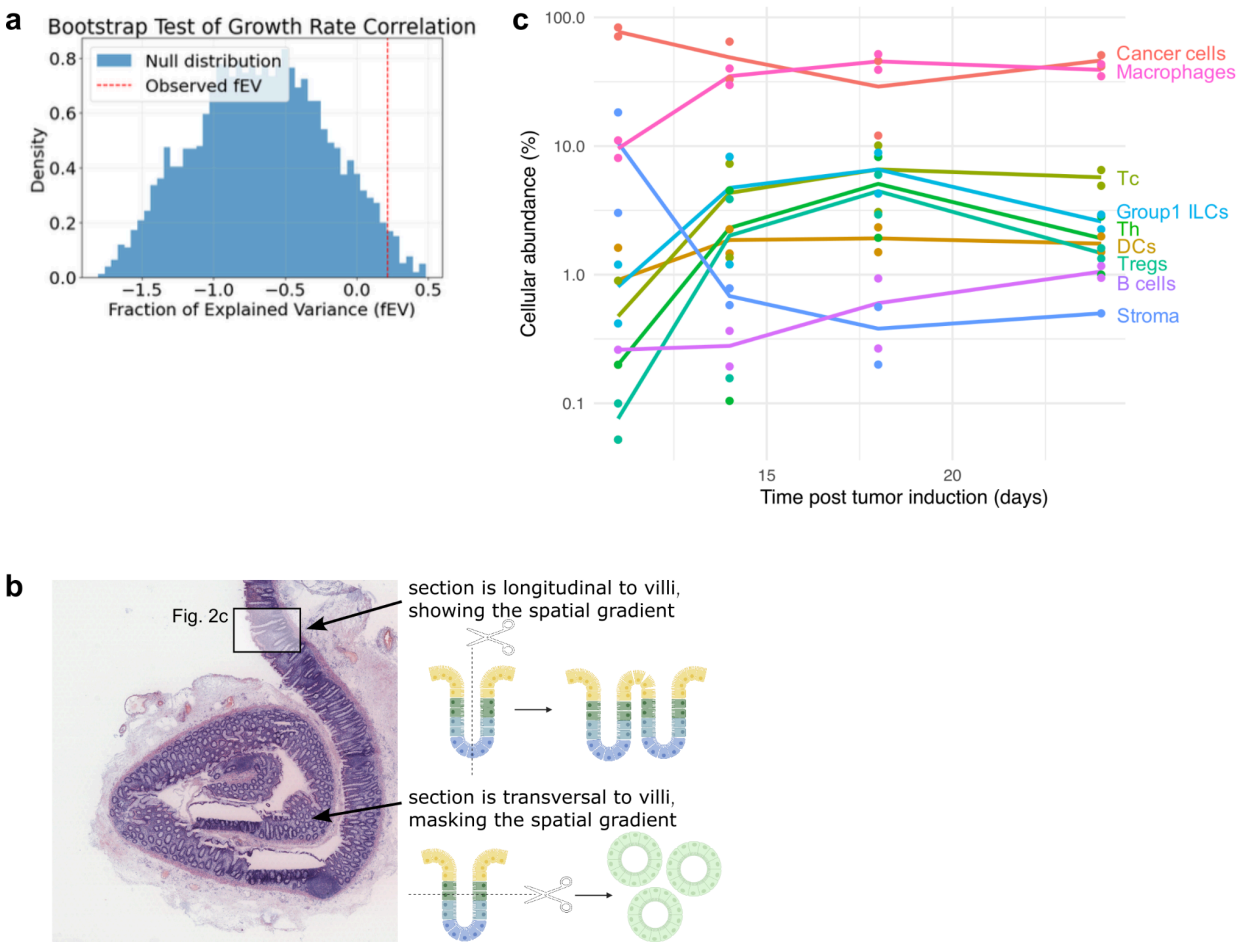

Figure S5 TIDYI recovers the known proliferation-death dynamics of homeostatic, expanding and shrinking tissues. (a) We tested whether TIDYI predicted measured tumor growth rates beyond what is expected by chance using a bootstrapping approach. To do so, bootstrap testing was performed by randomly permuting the TIDYI growth rates relative to the BLI growth rates and recalculating the fraction of explained variance (fEV) for each shuffle. The observed fEV was then compared to this null distribution to assess its statistical significance. **(b)** A region of the gut in which villi are sectioned longitudinally was selected to examine the spatial gradient of TIDYI proliferation and death signatures. There can be no spatial gradient in regions where villi were sectioned transversally. **(c)** In the longitudinal tumor scRNAseq data of Gsell et al., stromal cells are lost relative to cancer cells over time. Immune cells have high prevalence (~50% of all cells). Cell typing and temporal dynamics: original study.

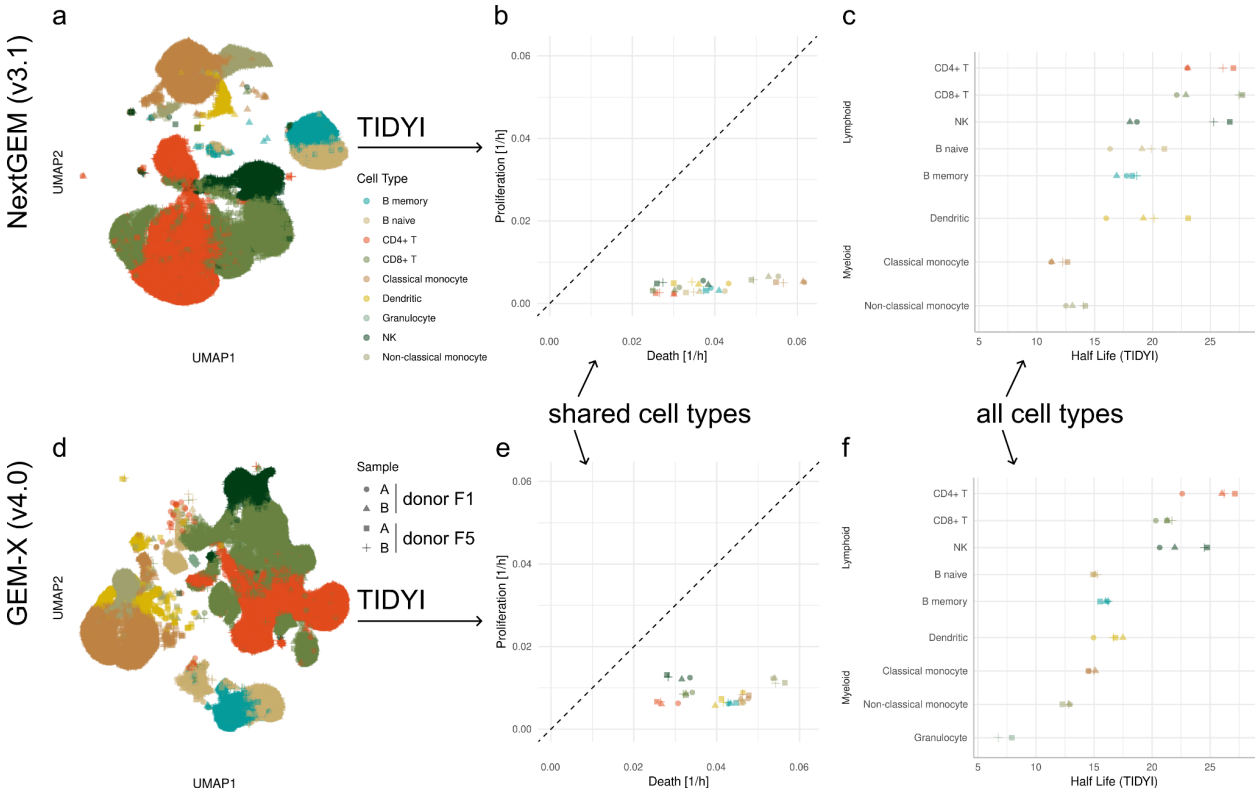

Figure S6 Performing TIDYI on human peripheral blood immune cells validates that immune cells proliferate little in the blood, that lymphoid cells are longer lived than myeloid cells, and that rate estimates are consistent across scRNAseq protocols and replicates. (a) UMAP projection of the single-cell transcriptional profiles of 50,766 cells. Color: cell type. Shape: donor and technical replicate. **(b)** Proliferation and death rates inferred by TIDYI suggest little proliferation among blood immune cells, consistent with their known genesis and proliferation in other compartments (bone marrow, peripheral infected tissue, lymph nodes, …). Dots: cell types in different donors and replicates. **(c)** TIDYI accurately estimates that myeloid cells are shorter lived than lymphoid cells. This is consistent with the role that lymphoid cells play in adaptive immune memory, thus requiring longer life spans than myeloid cells of the innate immune system. **(d-f)** Same for 95,666 human peripheral blood immune cells. Data: Elz et al.[11].

Table S1 Top 200 genes discriminating between live vs dying/dead cells across 6 cell cultures. The first 122 genes optimized test set accuracy in classifying dead cells. Score: z-score. p-value: t-test comparing expression in dying/dead vs live cells. Adjusted p-value: false-discovery rate (Benjamini-Hochberg).

	Gene symbol	Score (z-score)	Log2 fold change	p-value	Adjusted p-value
0	MT-ND4L	24.94066	0.95959103	5.65E-127	1.53E-122
1	MT-CO3	24.88137	0.9254645	1.61E-126	2.17E-122
2	MT-CO1	23.8767	0.8245061	3.24E-117	2.91E-113
3	MT-ATP8	23.284239	0.8656687	6.35E-112	2.85E-108
4	MT-ND6	23.006527	1.0387713	2.05E-109	6.93E-106
5	MT-CO2	22.984577	0.8703126	3.46E-109	1.04E-105
6	MTCO1P12	22.941647	0.90795314	5.38E-109	1.45E-105
7	MT-CYB	22.670128	0.83794755	1.98E-106	4.45E-103
8	MT-RNR1	22.348156	0.8836431	6.18E-104	1.19E-100
9	MT-ND5	21.741798	0.83021146	1.35E-98	1.66E-95
10	MT-RNR2	21.689856	0.8299637	2.78E-98	3.26E-95
11	MTND2P28	21.672709	0.832038	3.37E-98	3.79E-95
12	MT-ND1	19.866695	0.78721845	1.20E-83	5.42E-81
13	MT-TS2	19.166939	0.9251042	4.32E-78	1.32E-75
14	MT-ND3	18.832218	0.8161499	8.43E-76	2.39E-73
15	MT-ATP6	18.76423	0.7696822	3.05E-75	8.31E-73
16	MT-ND2	17.546812	0.75996107	2.27E-66	3.55E-64
17	MT-TM	15.35279	0.70243263	1.42E-51	1.04E-49
18	MT-ND4	15.244308	0.7167931	5.05E-51	3.60E-49
19	MT-TS1	14.309895	0.94017553	4.18E-45	2.16E-43
20	MT-TP	14.293876	0.666166	3.69E-45	1.91E-43
21	MTCO2P12	13.708907	0.77989906	1.00E-41	4.27E-40
22	MTCO3P12	13.448419	0.76466995	2.68E-40	1.07E-38
23	MT-TY	12.943311	0.88646805	2.07E-37	7.25E-36
24	MTATP6P1	12.369338	0.66289693	1.71E-34	5.20E-33
25	MT-TF	12.122069	0.7427994	3.64E-33	1.05E-31
26	MT-TL1	11.927076	0.71267945	3.42E-32	9.36E-31
27	MT-TE	11.26495	0.6301697	5.85E-29	1.36E-27
28	MTND6P3	11.076671	0.6378556	4.70E-28	1.05E-26
29	MT-TH	11.011988	0.5590276	9.26E-28	2.03E-26
30	MTND6P4	10.810295	1.0442448	9.65E-27	2.00E-25

31	LAMB1	10.526579	0.7131328	1.58E-25	3.07E-24
32	ITGA3	10.217605	0.49482155	3.43E-24	6.24E-23
33	APP	10.060534	0.46614748	1.64E-23	2.91E-22
34	MTRNR2L8	9.947344	0.7396765	5.21E-23	8.99E-22
35	NOMO2	9.42386	0.6343406	7.84E-21	1.21E-19
36	MTND1P23	9.305844	0.6270748	2.24E-20	3.39E-19
37	MTRNR2L12	9.303804	0.59469354	2.26E-20	3.40E-19
38	ATP6AP2	9.2750635	0.43595862	3.01E-20	4.49E-19
39	MALAT1	9.236557	0.49411455	4.16E-20	6.17E-19
40	MYADM	9.210878	0.45116267	5.31E-20	7.84E-19
41	PDIA3	9.134356	0.4066095	1.09E-19	1.57E-18
42	ASPH	9.087481	0.47924653	1.59E-19	2.29E-18
43	ABCC3	9.034723	0.8525512	2.74E-19	3.88E-18
44	TCIRG1	8.777149	0.55019224	2.54E-18	3.42E-17
45	MTRNR2L1	8.751813	0.7634108	3.28E-18	4.36E-17
46	COL18A1	8.620276	0.83178854	1.03E-17	1.34E-16
47	FKBP10	8.611877	0.8948793	1.08E-17	1.39E-16
48	NCLN	8.585982	0.52809614	1.33E-17	1.71E-16
49	TGFBI	8.560648	0.59600204	1.64E-17	2.09E-16
50	GANAB	8.547338	0.34933186	1.85E-17	2.36E-16
51	SCARB1	8.412076	0.6764148	5.86E-17	7.27E-16
52	LAPTM4B	8.284524	0.42062613	1.64E-16	1.97E-15
53	NPIPB5	8.254443	0.637717	2.19E-16	2.62E-15
54	MT-TN	8.212627	0.75102586	3.00E-16	3.56E-15
55	OS9	8.177175	0.38245997	4.00E-16	4.71E-15
56	CYBA	8.11758	0.3613018	6.46E-16	7.52E-15
57	MTCYBP18	8.0622835	0.74709266	1.06E-15	1.22E-14
58	PON2	8.06012	0.7561503	1.03E-15	1.19E-14
59	STT3B	8.058082	0.3722528	1.04E-15	1.20E-14
60	PCYOX1	8.049974	0.43203747	1.12E-15	1.29E-14
61	TMEM259	8.042963	0.47506782	1.18E-15	1.36E-14
62	SPP1	8.041185	0.9817146	1.22E-15	1.40E-14
63	CD81	8.006156	0.40931988	1.58E-15	1.79E-14
64	LENG8	7.875803	0.4394621	4.47E-15	4.94E-14
65	GLG1	7.819947	0.3960475	6.88E-15	7.49E-14
66	STRA6	7.8053575	1.3101159	8.35E-15	9.07E-14
67	MT-TL2	7.7987556	1.1414222	8.49E-15	9.21E-14
68	PRKCSH	7.776981	0.30870786	9.65E-15	1.04E-13
69	COL7A1	7.7704372	0.57351303	1.02E-14	1.10E-13

70	CD44	7.760179	0.29927182	1.10E-14	1.19E-13
71	MT-TV	7.7287717	0.45585826	1.37E-14	1.47E-13
72	MT-TD	7.726196	0.47536486	1.41E-14	1.51E-13
73	MT-TR	7.6781864	0.665416	2.10E-14	2.22E-13
74	AGRN	7.668081	0.49386352	2.24E-14	2.37E-13
75	PDIA4	7.6498723	0.36939606	2.56E-14	2.70E-13
76	COL6A2	7.639105	0.72567695	2.83E-14	2.96E-13
77	MTATP8P1	7.6362653	0.6694691	2.90E-14	3.04E-13
78	NUP210	7.6219625	0.9234732	3.24E-14	3.38E-13
79	SREBF1	7.6017346	0.6751768	3.75E-14	3.90E-13
80	TSPAN4	7.5230937	0.33681354	6.70E-14	6.87E-13
81	ACSL3	7.5162373	0.41336158	7.09E-14	7.25E-13
82	SLC2A1	7.4969044	0.377214	8.17E-14	8.32E-13
83	SLC38A10	7.450583	0.5574224	1.16E-13	1.17E-12
84	CA12	7.4269314	0.8226232	1.40E-13	1.40E-12
85	EBP	7.424861	0.37081903	1.40E-13	1.40E-12
86	MPDU1	7.4219723	0.32049125	1.43E-13	1.44E-12
87	CLSTN1	7.4065633	0.42617622	1.61E-13	1.61E-12
88	SPDYE2	7.3917265	0.66601056	1.82E-13	1.81E-12
89	PLPP2	7.373435	0.42702413	2.06E-13	2.04E-12
90	CRIM1	7.3727984	0.40225658	2.06E-13	2.04E-12
91	TMED7	7.348677	0.42884547	2.46E-13	2.42E-12
92	PLOD1	7.3374324	0.41133156	2.67E-13	2.62E-12
93	6-Mar	7.3277617	0.39597264	2.88E-13	2.81E-12
94	EMC10	7.3126154	0.5765065	3.27E-13	3.18E-12
95	MET	7.2953334	0.36855182	3.64E-13	3.53E-12
96	SPG7	7.292242	0.44407478	3.75E-13	3.63E-12
97	HSPG2	7.2915025	0.67540526	3.83E-13	3.70E-12
98	DCBLD2	7.287997	0.39023158	3.83E-13	3.70E-12
99	TSPAN3	7.2157974	0.37194735	6.47E-13	6.18E-12
100	GJA1	7.1967974	0.60162526	7.53E-13	7.17E-12
101	APMAP	7.165182	0.2984173	9.37E-13	8.87E-12
102	HSP90B1	7.1631985	0.28268912	9.54E-13	9.03E-12
103	TMEM245	7.1518197	0.35327798	1.03E-12	9.73E-12
104	PFAS	7.1477523	0.43256375	1.07E-12	1.01E-11
105	IGF2R	7.1220164	0.3735415	1.28E-12	1.19E-11
106	RPN2	7.1045446	0.2701013	1.45E-12	1.35E-11
107	VPS13C	7.1042624	0.5930632	1.46E-12	1.36E-11
108	RPN1	7.0929894	0.29219833	1.57E-12	1.46E-11

109	TMEM30A	7.0761943	0.36154273	1.77E-12	1.64E-11
110	AL390728.6	7.0689864	0.73511463	1.91E-12	1.77E-11
111	AC015813.1	7.062697	0.6184257	1.97E-12	1.82E-11
112	NEO1	7.0531073	0.68371034	2.13E-12	1.96E-11
113	SLC2A6	7.031217	0.58261555	2.45E-12	2.25E-11
114	LOXL2	7.0302763	0.3450516	2.45E-12	2.24E-11
115	COL5A2	7.0148234	0.9620949	2.81E-12	2.56E-11
116	CNTN1	7.003814	0.83903813	2.98E-12	2.72E-11
117	COL4A2	7.003591	0.4834653	2.97E-12	2.70E-11
118	GAA	6.99445	0.59573054	3.19E-12	2.89E-11
119	SDC1	6.9887333	0.44381607	3.28E-12	2.98E-11
120	NRCAM	6.965286	0.83912295	3.92E-12	3.53E-11
121	SNX14	6.964105	0.4222483	3.93E-12	3.54E-11
122	ADGRE5	6.963911	0.39028075	3.93E-12	3.54E-11
123	RDH11	6.9473915	0.299369	4.39E-12	3.93E-11
124	ZNF331	6.946303	0.5536565	4.51E-12	4.03E-11
125	FTX	6.94059	0.5810515	4.69E-12	4.19E-11
126	DST	6.9251714	0.33482784	5.13E-12	4.58E-11
127	TPP1	6.9209075	0.44217533	5.28E-12	4.71E-11
128	CD151	6.9087844	0.2850064	5.74E-12	5.10E-11
129	PLOD3	6.9066806	0.42770106	5.88E-12	5.22E-11
130	ADAM10	6.8867364	0.33553693	6.72E-12	5.95E-11
131	CCDC14	6.876796	0.48281178	7.23E-12	6.39E-11
132	HACD2	6.8622746	0.46557218	7.97E-12	7.02E-11
133	COL27A1	6.8594775	0.64095527	8.22E-12	7.23E-11
134	MT-TC	6.8525534	0.8579205	8.68E-12	7.60E-11
135	KDELR1	6.8379073	0.2837961	9.39E-12	8.20E-11
136	SYNGR2	6.831047	0.3589614	9.86E-12	8.60E-11
137	MT-TQ	6.8296747	0.65845674	1.00E-11	8.72E-11
138	GOLGA8B	6.811949	0.52658445	1.13E-11	9.77E-11
139	AC159540.2	6.7894893	0.7305338	1.32E-11	1.14E-10
140	SLC6A6	6.7756634	0.43850347	1.44E-11	1.24E-10
141	STEAP3	6.772553	0.42876396	1.48E-11	1.27E-10
142	LGALS3BP	6.7453837	0.2821858	1.77E-11	1.50E-10
143	PLOD2	6.7252493	0.41673213	2.03E-11	1.72E-10
144	HERC2P2	6.7093706	0.44912368	2.26E-11	1.90E-10
145	COCH	6.70466	1.0747436	2.41E-11	2.02E-10
146	ABHD2	6.703213	0.3707439	2.37E-11	1.99E-10
147	RTN3	6.690706	0.27206266	2.57E-11	2.16E-10

148	AHNAK2	6.6750507	0.40679723	2.84E-11	2.37E-10
149	GNS	6.67019	0.3644802	2.95E-11	2.46E-10
150	RNF149	6.6696258	0.41890666	2.95E-11	2.46E-10
151	STAG3L3	6.6641045	0.49372572	3.09E-11	2.57E-10
152	POR	6.652652	0.40281427	3.31E-11	2.75E-10
153	HAVCR1	6.6496415	1.23611	3.47E-11	2.88E-10
154	CXCL5	6.633603	0.87781686	3.77E-11	3.12E-10
155	MELTF	6.629326	0.563357	3.91E-11	3.23E-10
156	RRBP1	6.5920777	0.31717646	4.96E-11	4.06E-10
157	ABCC2	6.5910788	0.77014583	5.03E-11	4.12E-10
158	HKDC1	6.58556	0.6217197	5.24E-11	4.29E-10
159	DGCR2	6.568929	0.52207667	5.85E-11	4.76E-10
160	ASPM	6.5670395	0.5075888	5.87E-11	4.78E-10
161	SEMA4B	6.563051	0.54971886	6.06E-11	4.92E-10
162	P3H3	6.5558195	1.1140841	6.53E-11	5.30E-10
163	NOMO1	6.5383444	0.35878694	7.12E-11	5.75E-10
164	COL4A5	6.5358047	0.71881217	7.28E-11	5.88E-10
165	MTCO1P40	6.530147	0.6857234	7.57E-11	6.11E-10
166	ALDH1A1	6.5174813	0.8126325	8.08E-11	6.50E-10
167	C17orf62	6.51504	0.38556242	8.28E-11	6.65E-10
168	GALNT14	6.508517	0.6772806	8.67E-11	6.96E-10
169	CIT	6.4891295	0.48758036	9.87E-11	7.89E-10
170	ATP2A2	6.480929	0.2778898	1.03E-10	8.23E-10
171	LAMA5	6.4800997	0.5000577	1.04E-10	8.32E-10
172	LMF2	6.475717	0.42810002	1.08E-10	8.56E-10
173	CYP24A1	6.473982	0.68739307	1.09E-10	8.63E-10
174	PLBD2	6.4677167	0.41375807	1.13E-10	8.98E-10
175	NUCB1	6.466104	0.32559344	1.14E-10	9.05E-10
176	ABCC1	6.458512	0.4820879	1.20E-10	9.54E-10
177	ERBB2	6.45707	0.5388719	1.23E-10	9.73E-10
178	GTF3C1	6.4536853	0.43420154	1.24E-10	9.83E-10
179	PILRB	6.448906	0.8533556	1.31E-10	1.03E-09
180	SRPX	6.4419956	0.63123137	1.34E-10	1.05E-09
181	EPHB2	6.434918	0.44207788	1.40E-10	1.10E-09
182	AHNAK	6.421301	0.28040957	1.53E-10	1.20E-09
183	OSMR	6.409525	0.42888913	1.65E-10	1.29E-09
184	PROCR	6.408034	0.34780633	1.66E-10	1.30E-09
185	SLC27A2	6.407939	1.1675622	1.70E-10	1.33E-09
186	NPIPB4	6.389238	0.5906413	1.90E-10	1.48E-09

187	MIR16-2	6.3848343	0.79084325	1.96E-10	1.52E-09
188	MMP7	6.378044	0.9912295	2.05E-10	1.59E-09
189	ADPGK	6.3742228	0.40500113	2.07E-10	1.61E-09
190	TFRC	6.372249	0.25689417	2.10E-10	1.63E-09
191	HACD3	6.3692036	0.27643642	2.14E-10	1.66E-09
192	ARHGAP11B	6.360773	0.54680663	2.28E-10	1.76E-09
193	ARL6IP1	6.358463	0.32091114	2.28E-10	1.76E-09
194	AKR1C2	6.3429327	0.7793359	2.52E-10	1.94E-09
195	FN1	6.3423433	0.42334434	2.54E-10	1.95E-09
196	CPD	6.333567	0.3209834	2.68E-10	2.06E-09
197	AKR1B10	6.3118224	0.78388387	3.07E-10	2.35E-09
198	ELOVL5	6.2931147	0.2809626	3.49E-10	2.66E-09
199	TMEM51	6.258672	0.6146429	4.38E-10	3.32E-09

Table S2: Software and versions

Software/package	version	Company	City	State	Country
Cellpose	2.2.2				
CellProfiler	4.2.1				
R	4.0.3				
Rstudio	1.3.1073				
Zen Blue	3.3	Zeiss	Oberkochen		Germany
Zen Blue	3.5	Zeiss	Oberkochen		Germany
Axiovision	4.8	Zeiss	Oberkochen		Germany
Excel	2016	Microsoft			
Omega	1.11	BMG Labteck	Ortenberg		Germany
Inkscape	1.0.2-2	Inkscape			
ggplot2	3.3.5				
tidyverse	1.3.1				
plotly	4.10.0				
ggpubr	0.4.0				
readxl	1.3.1				
readr	2.1.2				

Table S3:

Product	Reference	Supplier	City	State	Country
MycoXpert	MYX_B	Nordic Biolabs	Taby		Sweden
DMEM/HIGH with 4.0mM L-glut, with Sodium Pyruvate	SH30243.LS	Nordic Biolabs	Taby		Sweden
HyClone FBS, EU approved, Heat Inactivated, South American	SV30160.03HI	Nordic Biolabs	Taby		Sweden
Penicillin-Streptomycin Solution	SV30010	Nordic Biolabs	Taby		Sweden
MDA-MB-231	ATCC-HTB-26	LGC	Teddington		UK
4T1; Mammary Tumor; Mouse (Mus musculus)	ATCC-CRL-2539	LGC	Teddington		UK
CELLTRACE CFSE	C34554	thermoScientific	ThermoScientific	Waltham	MA
PBS 1X 0.0067 M PO4, without Ca, Mg, Phenol Red, 6x1000 ml	SH30256.LS	Nordic Biolabs	Taby		Sweden
TC flask with Filter cap 75cm2 X2	90076	Nordic Biolabs	Taby		Sweden
TC Microplate 6 well, flat bottom, 4/bag	92406	NordicBiolabs	Taby		Sweden
PACLITAXEL	Y0000698	MERK	Kenilworth	NJ	USA
Countess™ Cell Counting Chamber Slides	C10312	ThermoScientific	Waltham	MA	USA
Falcon® 5 mL Round Bottom Polystyrene Test Tube, with Cell Strainer Snap Cap, 25/Pack, 500/Case	352235	Fisher Scientific	Waltham	MA	USA
Annexin V APC Ready Flow Conjugate	R37176	thermoScientific	Waltham	MA	USA
BOBO™-3 Iodide (570/602), 1 mM solution in DMSO	B3586	thermoScientific	Waltham	MA	USA
Chromium Next GEM Single Cell 3' GEM, Library & Gel Bead Kit v3.1, 4 rxns	PN-1000128	10X Genomics	Pleasanton	CA	USA

Table S4:

	MCF7_REF	MCF7_A	MCF7_L	MCF7_R	MDA-MB-231_REF	MDA-MB-231_A	MDA-MB-231_L	MDA-MB-231_R	MDA-MB-231_S
D7S820	8.9	8.9	8.9	8.9	8.9	8.9	8.8	8.8	8.8
CSF1PO	10	10.1	10.1	10.1	12.13	12.13	13.13	13.13	13.13
TH01	6	6,8,9	6.6	6.6	7,9,3	7,9,3	7,9,3	7,9,3	7,9,3
D13S317	11	11.11	11.11	11.11	13.13	13.13	13.13	13.13	13.13
D16S539	11.12	11.12	11.12	11.12	12.12	12.12	12.12	12.12	12.12
vWA	14.15	14.15	14.15	14.15	15.19	15.19	15.15	15.15	15.15
TPOX	9.12	9.12	9.12	9.12	8.9	9.9	8.9	8.9	9.9
AMEL	X,X	X,X	X,X	X,X	X,X	X,X	X,X	X,X	X,X
D5S818	11.12	11.12	12.12	12.12	12.12	12.12	12.12	12.12	12.12

References

1. Mahmoud, L. *et al.* Microscopy-based phenotypic monitoring of MDA-MB-231 spheroids allows the evaluation of phenotype-directed therapy. *Exp. Cell Res.* **425**, 113527 (2023).
2. Stringer, C., Wang, T., Michaelos, M. & Pachitariu, M. Cellpose: a generalist algorithm for cellular segmentation. *Nat. Methods* **18**, 100–106 (2021).
3. Hagemann-Jensen, M., Ziegenhain, C. & Sandberg, R. Scalable single-cell RNA sequencing from full transcripts with Smart-seq3xpress. *Nat. Biotechnol.* **40**, 1452–1457 (2022).
4. Hagemann-Jensen, M., Ziegenhain, C. & Sandberg, R. Smart-seq3xpress. https://www.protocols.io/view/smart-seq3xpress-dxcv7iw6 (2025).
5. Hawkins, E. D. *et al.* Measuring lymphocyte proliferation, survival and differentiation using CFSE time-series data. *Nat. Protoc.* **2**, 2057–2067 (2007).
6. Gsell, L. *et al.* Multi-cellular phenotypic dynamics during the progression of breast tumors. 2025.04.16.649085 Preprint at https://doi.org/10.1101/2025.04.16.649085 (2025).
7. Halprin, K. M. Epidermal “turnover time” - a re-examination. *Br. J. Dermatol.* **86**, 14–19 (1972).
8. Gelfant, S. The cell cycle in psoriasis: a reappraisal. *Br. J. Dermatol.* **95**, 577–590 (1976).
9. Breda, J., Zavolan, M. & van Nimwegen, E. Bayesian inference of gene expression states from single-cell RNA-seq data. *Nat. Biotechnol.* **39**, 1008–1016 (2021).
10. Traag, V. A., Waltman, L. & van Eck, N. J. From Louvain to Leiden: guaranteeing well-connected communities. *Sci. Rep. 2019 91* **9**, 1–12 (2019).
11. Elz, A. E. *et al.* Evaluating the practical aspects and performance of commercial single-cell RNA sequencing technologies. Preprint at https://doi.org/10.1101/2025.05.19.654974 (2025).